

Progress in China's Lunar Exploration Program*

ZOU Yongliao XU Lin WANG Qin

(National Astronomical Observatories, Chinese Academy of Sciences, Beijing 100012)

Abstract Chang'E-1 and Chang'E-2 of China's Lunar Exploration Program (CLEP) have successfully achieved their mission. At the present time, only Chang'E-3 is still in operation, which was successfully launched on December 2, 2013. Chang'E-3 probe is the third robotic lunar mission of CLEP, which consists of a lander and a rover, with eight payloads on board the spacecraft. Up to December 21, 2015, more than 2.86 TB raw data were received from these instruments onboard Chang'E-3 probe. A series of research results have been achieved. This paper gives a detailed introduction to the new scientific results obtained from Chang'E-3 missions.

Key words China's Lunar Exploration Program, Chang'E-3, Scientific results

Classified index P 148

1 Introduction

A total of three lunar spacecrafts of Chinese Lunar Exploration Program (CLEP) have been launched. Chang'E-1 and Chang'E-2 have successfully achieved the mission's science goals^[1-16]. Currently, Chang'E-3 is still in operation, which was successfully launched on December 2, 2013, and soft-landed on December 14, 2013. Chang'E-3 is the third robotic probe of CLEP, which consists of a lander and a rover (Yutu). There are eight scientific payloads onboard Chang'E-3: the Landing Camera (LCAM), the Terrain Camera (TCAM), the Extreme Ultraviolet Camera (EUVC) and the Moon-based Ultraviolet Telescope (MUVT) onboard the lander; the Panoramic Camera (PCAM) and the Visible/Near-Infrared Imaging Spectrometer (VNIS), the Active Particle-induced X-ray Spectrometer (APXS) and the Lunar Penetrating Radar

(LPR) on the rover Yutu. Their main scientific goals include: investigating the lunar local surface topography, geological structure and chemical compositions, monitoring the structure and dynamics of the Earth's plasmasphere, and conducting Moon-based astronomical observations.

Up to December 21, 2015, more than 2.86 TB raw data were received from these instruments onboard Chang'E-3. These raw data were pre-processed by channel processing, unpacked, calibrated and corrected, and so on, and produced data which scientists can use. The various data processing methods have provided scientists with help in further research.

LCAM and TCAM on the lander, and PCAM on the rover were used to investigate the surface topography and geological structure around the landing area. Through systematical processing of the data obtained by LPR, VNIS and APXS, we obtained the data on

* Supported by the Key Research Program of the Chinese Academy of Sciences (KGZD-EW-603)

Received May 31, 2016

E-mail: xul@nao.cas.cn

chemical composition and mineral abundance of lunar soil at the landing site and the superficial structure of lunar regolith and crust. It is the first attempt to explore the lunar subsurface structure by using high-resolution LPR. In addition, EUVC and MUVT on the lander made observations of the terrestrial plasmasphere and stars.

2 Preliminary Scientific Results for China's Lunar Exploration Program

2.1 Lunar Rover Yutu has Revealed the Volcanic History of the Imbrium Basin

Scientists have found that the data from LPR, VNIS and APXS can reveal large volcanic eruptions extending to 2500 Ma ago, probably induced by the local enrichment of radioactive elements in the landing area. In addition, the lunar regolith layer may be thicker than the previous estimates. These results provide important scientific constraints on the volcanic history of the Imbrium basin and the evolution of the Moon.

During the first 2 months, Yutu successfully carried out two APXS and four VNIS analyses on the lunar soils and performed a 114-meter-long LPR profile along the rover track in the landing area^[17–18] (see Figure 1).

2.1.1 Major and Trace Elements of Lunar Soils

The APXS of the rover Yutu generates X-ray by the artificial radioactive elements as the source. When the lunar soil is irradiated by the X-ray beam, it will emit X-ray fluorescence. Based on the intensities of X-ray fluorescence, the chemical composition of the lunar soil can be calculated. The background of X-ray fluorescence is very low when using an X-ray beam as source. Therefore, the APXS of the rover Yutu can detect not only the major elements, such as Mg, Al, Si, Ca, Ti, K, Fe and Cr, but also 4 trace elements,

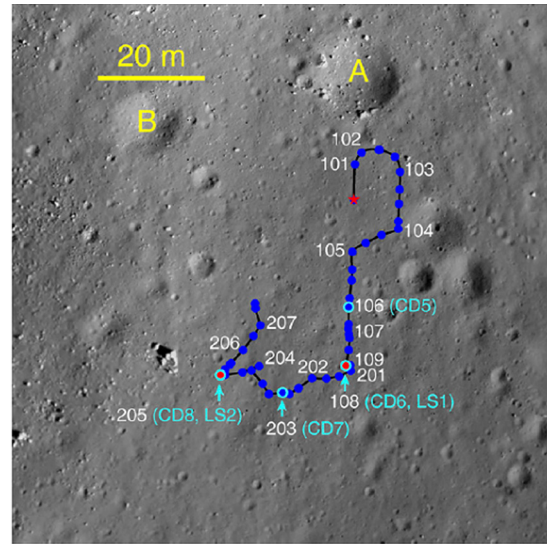


Fig. 1 Chang'E-3 landing site and the rover Yutu's track. The red star represents the landing position.

A and B represent two large impact craters.

The black line is the track of Yutu. LS1 and LS2 are positions of 2 APXS analyses, and CD5–8 are positions of 4 VNIS analyses

such as Sr, Y, Zr and Nb. According to the APXS data, the team obtained the contents of the 12 elements in the measured lunar soils (Table 1). In order to improve the accuracy the results, the team carried out a number of calibration experiments on 10 rock standards in laboratory, and established a complete data processing method.

The outer most lunar surface is covered by a thin layer of regolith due to 20–40 billion years long impact of numerous asteroids. The regolith measured by the Yutu can actually represent the underlying rock, which is a distinct type of mare basalt based on the APXS data. Compared with the Apollo and Luna soil samples, these soils are rich in Fe and Ti contents and poor in Al contents. In addition, they are enriched in K, Zr, Y and Nb, indicating assimilation of 10%–20% of the KREEP component—last remnants of lunar magma ocean, highly enriched in radioactive and incompatible elements, phosphorous, rare Earth elements and potassium. Thus, the basalt could be derived *via* partial melting of ilmenite-rich mantle

Table 1 Chemical compositions of the lunar soil measured by APXS

sample	lunar soil 1 (wt%)	lunar soil 2 (wt%)
SiO ₂	42.8	43.2
MgO	9.9±1.5	8.9±1.9
Al ₂ O ₃	11.5±0.9	10.5±1.0
K ₂ O	0.18±0.01	0.15±0.01
CaO	10.4±0.3	10.9±0.4
TiO ₂	4.0±0.2	4.3±0.2
FeO	21.3±1.7	22.1±1.9
total	100.0	100.0
Cr/ppm	877±162	825±161
Sr/ppm	139±19	198±29
Y/ppm	34±10	54±13
Zr/ppm	200±26	168±49
Nb/ppm	13±2	14±10

reservoir, then assimilated by the residual KREEP layer crust as it ascended, finally erupted into the Imbrium basin.

2.1.2 Mineral Abundances and Optical Maturity Index

The research team obtained the mineral abundances and optical maturity index of the lunar soils based on the VNIS data. The VNIS, mounted at the front of the Yutu, can acquire the visible to near-infrared spectra of the surface soils and exposed rocks in the landing area. Compared with the previous orbital detections, the VNIS of Yutu provided the highest spatial resolution. However, it showed significant shadow effect due to the observation angle and surface roughness. The team presented a method to effectively correct the shadow effect, decoded the spectral data of VNIS, and obtained iron and titanium contents, mineral abundances and optical maturity index of the lunar soils. The calibrated spectra with typical characteristics of space weathering are similar to that of the mare soil samples, and display lower reflectance than highland soils. In addition, the 4 VNIS analyses have variable optical maturity. The optical maturity and reflectance tend to increase towards the lander,

probably reflecting that the upper most surface soil was blown away during the landing process.

2.1.3 A Thicker Lunar Regolith Layer than Expected

Yutu's LPR is the first radar deployed on the lunar surface since human exploration of the Moon. The team acquired the thickness and structure of the lunar regolith, and identified three layers of basalt and their thickness based on the LPR data. The LPR has two working frequency: high frequency channel of 500 MHz with detection depth of tens of meters and resolution of > 30 cm; low frequency channel of 60 MHz with detection depth of hundreds of meters and resolution at meter level. In order to obtain accurate and clear results, instantaneous frequency spectrum analysis and migration method in the field of seismic exploration have been used for data processing.

The lunar was covered by a homogeneous dust layer, which is about 0.7 m thick. This result is consistent with those of borehole core method by the Apollo program. The thickness of the lunar regolith in the mare area was previously estimated to about 2 to 4 m because this region with young ages should have a thinner regolith layer. However, the LPR results indicate a regolith thickness of about 5 m, which is significantly higher than previous estimation. Although the thick regolith layer may be partially attributed to the ejecta deposits from a large crater close to the landing site, high resolution topography images show that this impact is limited. Since the lunar soil is the most important reservoir of helium-3 and hydrogen, this result is very important for future exploitation of lunar resources (Figure 2).

2.1.4 The Moon is Still Active in Its Old Age

Another important achievement is the identification of three reflecting interfaces in the deep interior, based on which, thicknesses of 3 suits of basalts can be calculated. The thickness of the latest basalt unit is about 195 meters, showing that there were still huge basalt magma eruptions during lunar old age (about 2500 million years ago). The Moon experienced aste-

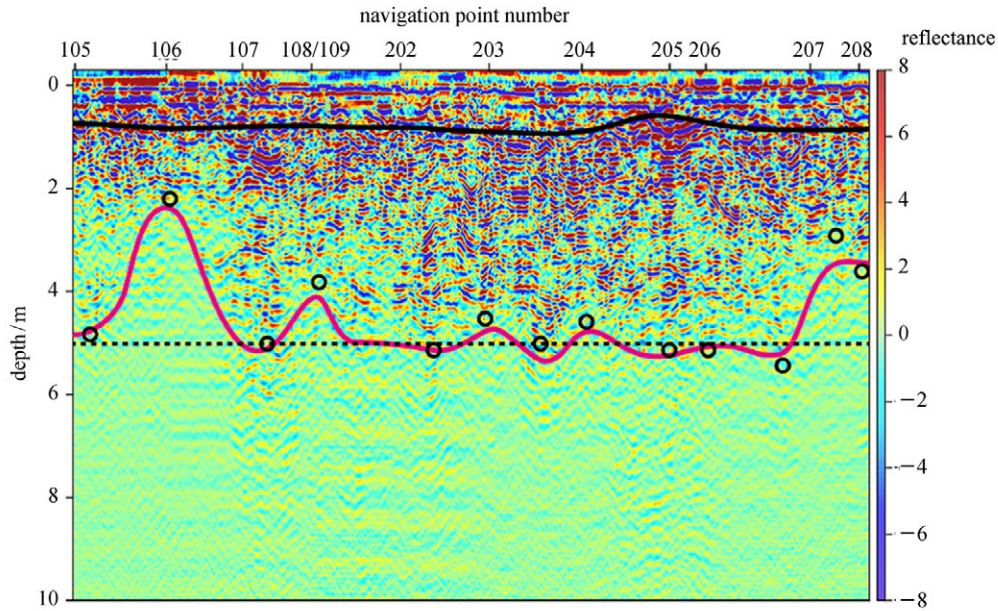


Fig. 2 Migration result of high frequency channel of LPR. Bold black and red curves denote the lunar soil sublayer and regolith bottoms, respectively. Bold black circles are the depths of lunar regolith picked up from the key traces by time-frequency analyses after migration. The dashed black line (at 5 m depth) denotes the best depth estimation of the lunar regolith at the research area

roid bombardment at about 3.9 billion years, forming basins with different sizes on the surface. These basins were then filled by basaltic magma at about 3.8–3.1 Ga. After that, the Moon entered its old age, and the magmatism tended to stop. However, the Yutu data showed that strong volcanic activity of the mare area lasted until 2.5 Ga. The lunar soils of the landing site contain 10%–20% of KREEP component, indicating assimilation of the residual KREEP layer crust as the magma ascended. The KREEP is enriched in radioactive elements, which provided the major energy of the long term magmatism (Figure 3).

2.2 Layered Subsurface Structure and Complex Geological History of Chang'E-3 Landing Site are Revealed

The Lunar Penetrating Radars (LPR) onboard Yutu rover has firstly detected the subsurface structure of the landing site. The shallow surface stratigraphic structure over the Chang'E-3 landing site was systematically studied based mainly on the high-frequency LPR data, along with the optical images acquired by the descending and terrain cameras^[19–22]. The re-

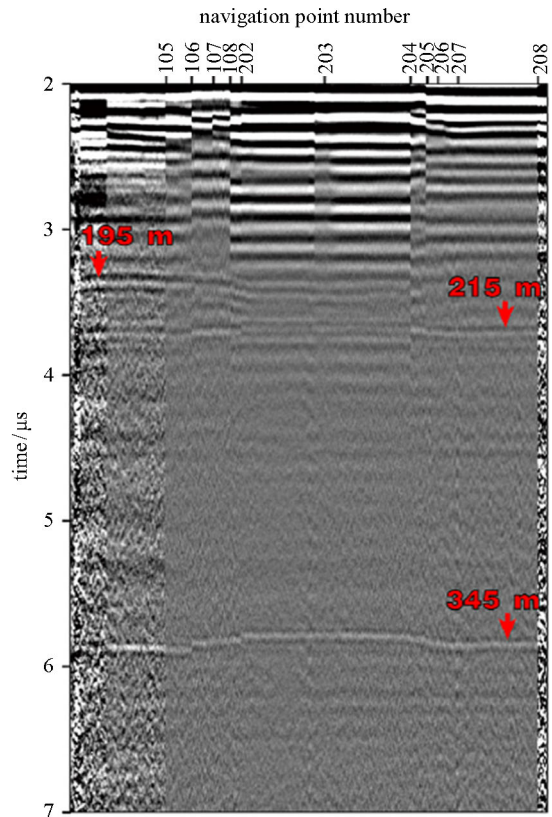


Fig. 3 LPR profile of low frequency channel, showing two reflection interfaces at 195 m, 215 m and 345 m, respectively

sults reveal four major stratigraphic zones from the surface to a depth of ~ 20 m: a layered reworked zone (< 1 m), an ejecta layer (about 2–6 m), a paleo-regolith layer (about 4–11 m), and the underlying mare basalts. Combining with the regolith thickness estimation, the LPR observations indicate a larger accumulation rate of lunar surface regolith as compared with previous estimation at the Apollo landing sites (Figure 4).

Low-frequency radar obtained deeper structure information. Data inversion and interpretation, com-

binning with local and regional geological characteristics, six more layered rock units have been revealed: 8–35 m basalts, 35–45 m paleo-regolith, 45–140 m massive basalts, 140–240 m layered volcanic/pyroclastic rocks, 240–360 m and below 360 m massive basalts. The upper layer Eratosthenian basalts (~ 2.5 Ga) extend to a depth of ~ 35 m, which is filled above a ~ 10 m thick paleo-regolith layer formed at the surface of underlying Imbrian basalts (~ 3.3 Ga) (Figure 5). It is suggested that there is at least three Imbrian volcanic eruption events to the

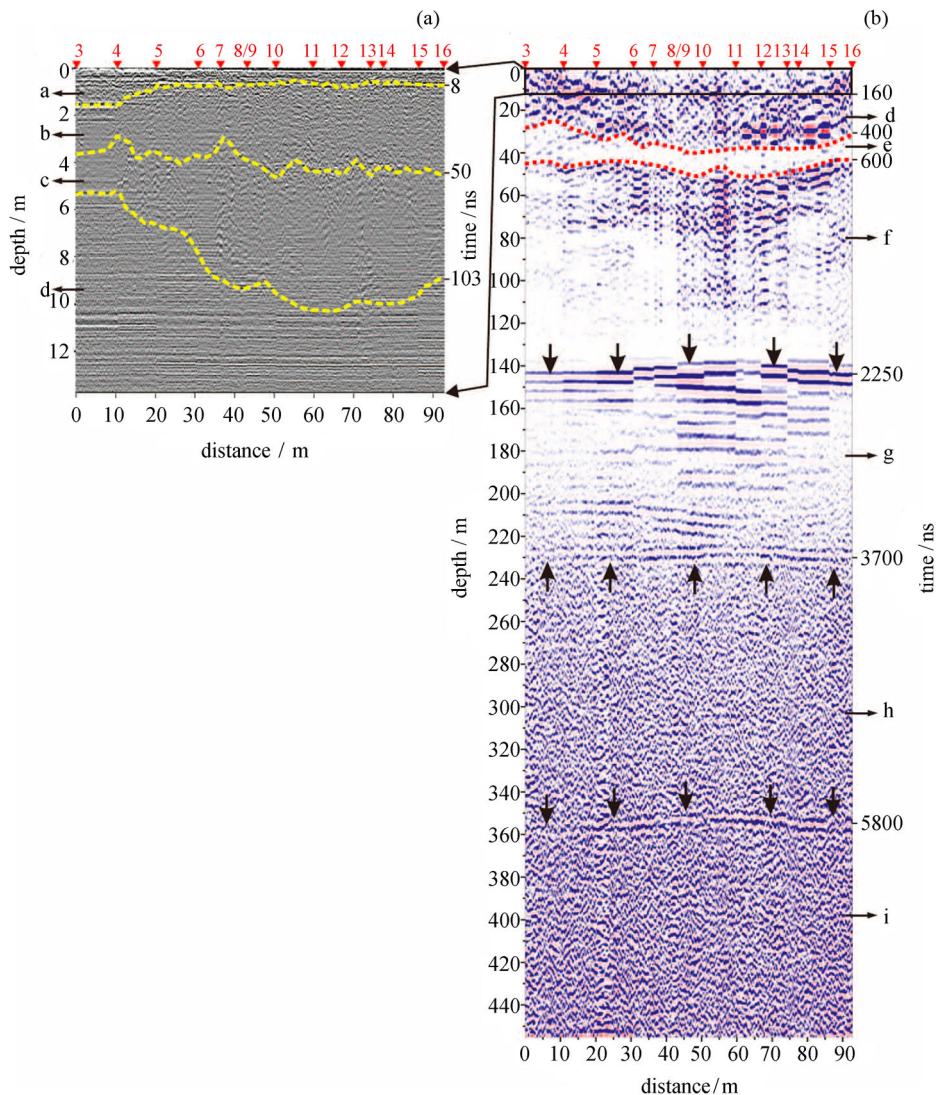


Fig. 4 Results and interpretations of the LPR Channel-2B and Channel-1 data. (a) Channel-2B. (b) Channel-1. The interpreted interfaces are marked as dashed lines and arrows and are labeled from a to i. The time-to-depth conversion for the LPR profiles are based on the empirical dielectric constant ϵ . $\epsilon = 3$ (2) the Channel-2B data, and the dielectric constants (17) for Channel-1 data are shown in Table 1

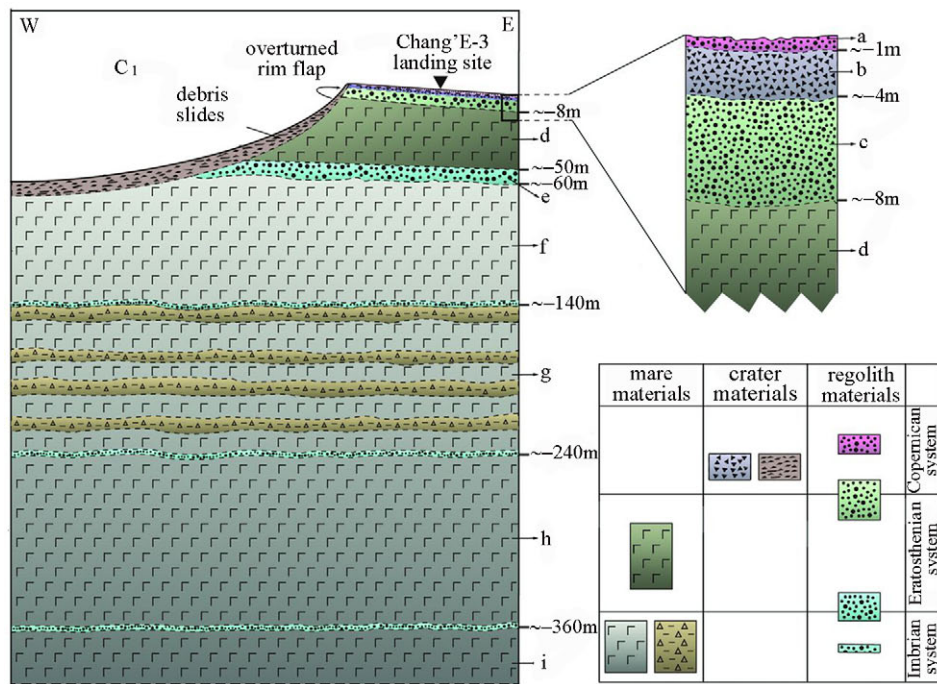


Fig. 5 Sketched geological cross section and an inferred profile of the Chang'E-3 landing site. Yutu has detected seven subsurface interfaces, which formed from Imbrian to Copernican. Letters a to i indicate interpreted subsurface layers based on LPR data

depth of ~400 m. These layered lava and pyroclastic rocks are inter-bedded by space weathering formed regolith during the interval of volcanic events. Relatively accurate knowledge on regolith thickness and shallow surface structure of lunar crust was obtained, which provides reliable structural constraints to study the lunar volcanism history and estimate the reserve of lunar He-3 resources.

2.3 A New Rock Type on Lunar

Surface is Discovered

According to Lunar Magma Ocean (LMO) model, the mineral composition and their spatial distribution on lunar surface are determined by the initial global differentiation and later magmatic activities. The elemental and major mineral (olivine, pyroxene, plagioclase and ilmenite) contents across lunar surface are keys to understand lunar evolution history. Comprehensive study of the datasets obtained from Active Particle-induced X-ray Spectrometer (APXS) and Visible and Near-infrared Imaging Spectrometer

(VNIS) aboard rover Yutu (Figure 6 and Figure 7), we obtained the compositional and mineralogical information of lunar rock/soil at Chang'E-3 landing site. The analysis indicates a new type of mare basalt rich in olivine and ilmenite within the “Guang Han Gong” that has not been sampled by previous Apollo and lunar missions and lunar meteorite collections. Thus Chang'E-3 landing site (“Guang Han Gong”) has become a new calibration site with ground truth for lunar remote sensing studies, providing critical constraints for later-stage lunar volcanism as well as the mechanism of magmatic evolution^[23].

2.4 Space Weathering Process and Products are Quantify Constrained

Lunar surface regolith carries important information on space weathering processes, the lunar environment and is very important for lunar explorations^[24–25]. On the first lunar day after the rover deployment, the onboard Panorama Camera (PCAM's) captured the first in-situ lunar opposite ion effect since the

Apollo era. The in-situ lunar phase curve, covering the phase angle range from 2° to 141° , was extracted from the PCAM's images and by performing photometric inversions the physical properties of the upper regolith have been inferred. The major results include: the surface regolith porosity is around photometric inversions the physical properties of the upper regolith have been inferred. The major 0.68, the regolith grains may be more transparent than the average maria, and the average slope angle ranges from 11° to 18° which is also smaller than the average maria.

2.5 EUV Camera—An Overview on Observations of the Earth's Plasmasphere with EUV Camera Onboard Chang'E-3

The Earth's plasmasphere, composed of dense and cold plasma coming from the ionosphere, has been observed for more than six decades since 1950s. Space missions play important roles in explorations of the plasmasphere. The Extreme Ultraviolet Imager working at a wave band of 30.4 nm on the Imager for Magnetopause-to-Aurora Global Exploration (IMAGE) satellite brings us great knowledge althou-

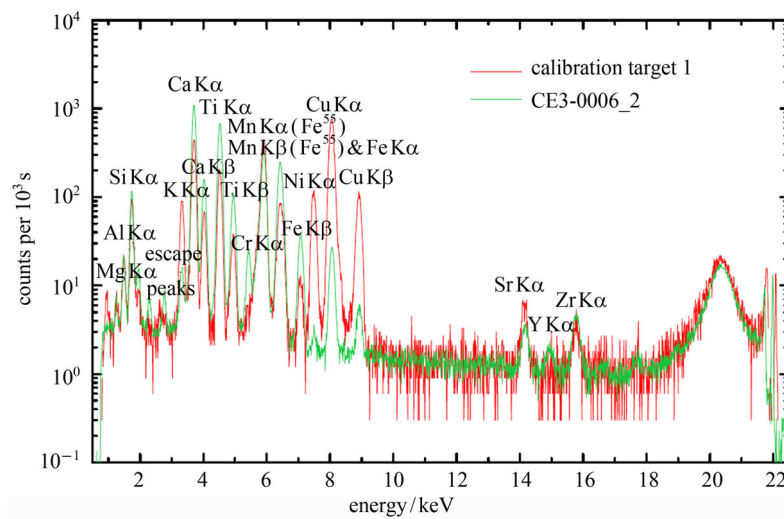


Fig. 6 X-ray spectrum and chemical compositions of Chang'E-3 soils from APXS. APXS spectrum CE3-0006_2 overlain on the calibration spectrum

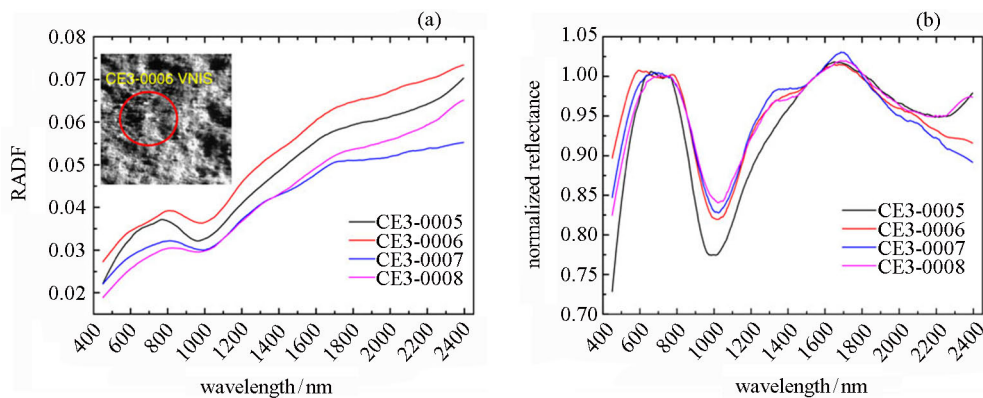


Fig. 7 Visible-NIR spectral properties and mineral chemistry of Chang'E-3 soils from VNIS. (a) Combined VNIS spectra (450—2400 nm) from sites 0005, 0006, 0007 and 0008. The inset image is from site CE3-0006 of the VNIS (450—950 nm) image mode at 750 nm. The dashed circle indicates the region measured by the VNIS-point spectral mode (900—2400 nm). (b) VNIS spectra after continuum removal

gh this mission ended several years ago. In its elliptical orbit, 90° inclination with an apogee altitude of $7 R_e$ and perigee of 1000 km, IMAGE can only make observations in polar views with short exposure time. In 2008, the Telescope of Extreme Ultraviolet (TEX) working at a wave band of 30.4 nm on a Japanese satellite named KAGUYA provided the first sequential images of the plasmasphere in meridian views. Due to some problems in the instrument, TEX can only provide observational data with a half field of view during its short life time.

In order to observe the Earth's plasmasphere in a global scale meridian view, a moon based EUV Camera (EUVC) made observations at a wave band of 30.4 nm and with a field of view of 15° during the period of December 2013 to June 2014. On the top deck of Chang'E-3, this camera obtained more than 1000 images of the Earth's plasmasphere with an angular resolution of 0.1° and a temporal resolution of 10 minutes within some time intervals of Moon's day. More than 20 hours continuous observations were made in February, April and May of 2014, respectively. Combining with other space observations, we study the plasma density configuration, velocity fields and global structure evolution in the Earth's plasmasphere.

By reconstructing the global plasmaspheric configuration based on the EUVC images observed during 20–22 April 2014, we show that in the observing period, the plasmasphere had three bulges which were located at different geomagnetic longitudes. The inferred midnight transit times of the three bulges, using the rotation rate of the Earth, coincide with the expansion phase of three substorms, which implies a causal relationship between the substorms and the formation of the three bulges on the plasmasphere. Instead of leading to plasmaspheric erosion as geomagnetic storm does, magnetospheric substorms initiated on the night side of the Earth cause local inflation of plasmasphere in the midnight region.

The plasmopause locations determined from the EUVC images and the auroral boundaries determined from the Defense Meteorological Satellite Program

(DMSP) Special Sensor Ultraviolet Spectrographic Imager (SSUSI) images are used to investigate the plasmaspheric evolutions during substorms. The most important finding is a nightside pointing plasmaspheric plume observed at 23:05 UT on 21 April 2014 under very quiet geomagnetic conditions. High correlations between the plasmopause evolutions and the auroral signatures exist during substorms. After substorm onset, the plasmopause erosion and the equatorward expansion of the auroral oval occur almost simultaneously in both MLT and UT, and then both the erosion and the expansion propagate westward and eastward. The enhanced convection during substorms or Earthward propagation of dipolarization fronts produces plasmasphere erosion and MLT propagations, and the substorm dipolarization causes pitch angle scattering of plasma sheet electrons and the resulting precipitation excites aurora emissions at the same time^[26–34].

2.6 LUT Observations

By using the LUT observations with extremely low stray light pollution caused by sunshine, Wang *et al.*^[35] reported an unprecedented upper limit of the content of the OH radicals in lunar exosphere through the in-situ measurements of the diffuse sky background. The column density and surface concentration of the OH radicals are obtained to be $< 10^{11} \text{ cm}^{-2}$ and $< 10^4 \text{ cm}^{-3}$, respectively, basing upon the resonance fluorescence emission at 3081 Å. This results is the best knowledge of the OH content in the lunar exosphere to date (being lower than the previously reported value given by HST by about two orders of magnitude), and is close to the prediction of the sputtering model.

Spectral datasets from NUV to optical band were constructed by Wang *et al.*^[36] for 44 International Ultraviolet Explorer (IUE) standards, because of the LUT's relatively wide wavelength coverage. With the spectral datasets, Wang *et al.*^[37] shows a highly stable photometric performance during LUT's 18-month's operation. The magnitude zero point is determined to be $17.53 \pm 0.05 \text{ mag}$, which is independent of the spec-

tral type of the standard from which the magnitude zero point is determined. Qi *et al.*^[38] presented an astrometric solution of LUT to calibrate the basic information (attitude, CCD constants, *etc.*) of LUT, not only for the accurate pointing and tracking of celestial objects but also for target detection on CCD images.

Meng *et al.*^[39] developed a dedicated data processing pipeline for LUT point observations that monitor variable objects in NUV band. The procedures of the pipeline include stray light removing, astrometry, flat fielding employing superflat technique, source extraction and cosmic ray rejection, aperture and PSF photometry, aperture correction, and catalogues archiving, *etc.* The resulted photometric accuracy is typically ~ 0.02 mag for LUT 10 mag stars (30 s exposure).

Qian *et al.*^[40] analyzed the NUV light curve of short-period eclipsing binary GQ Dra observed by LUT, which suggests a long-term increase of orbital period at a rate of $(3.48 \pm 0.23) \times 10^{-7} \text{ d}\cdot\text{a}^{-1}$ and a mass transfer rate of $(9.57 \pm 0.63) \times 10^{-8} M_{\odot}\cdot\text{a}^{-1}$. Zhu *et al.*^[41] obtained a photometric solution of semi-detached binary V548 Cygni in NUV band. The solution suggests that there are three cyclic variations that are interpreted by the light travel-time effect *via* the presence of three additional stellar companions. The photometric solution of the well-known Algol-type binary TW Dra was obtained by Liao *et al.*^[42] by analyzing the first NUV light curve obtained by LUT. Based on 589 available data spanning more than one century, the authors identify three cyclical changes. The two cyclical changes with short periods can be explained as the result of two circum-binary companions orbiting around TW Dra.

Acknowledgements We thank Lin Yangting, Yang Wei, Hu Sen, Xiao Long, Ling Zongcheng, Wang Huaning, He Han, Wei Jianyan, Wang Jing for providing reference materials.

References

- [1] CHEN B, SONG K F, LI Z H, *et al.* Development and calibration of the Moon-based EUV camera for Chang'E-3 [J]. *Res. Astron. Astrophys.*, 2014, **14**: 1654
- [2] DAI S, SU Y, XIAO Y, *et al.* Echo simulation of lunar penetrating radar: based on a model of inhomogeneous multilayer lunar regolith structure [J]. *Res. Astron. Astrophys.*, 2014, **14**: 1642
- [3] FANG G Y, ZHOU B, JI Y C, *et al.* Lunar penetrating radar onboard the Chang'E-3 mission [J]. *Res. Astron. Astrophys.*, 2014, **14**: 1607
- [4] FENG J Q, LIU J J, HE F, *et al.* Data processing and initial results from the CE-3 Extreme Ultraviolet Camera [J]. *Res. Astron. Astrophys.*, 2014, **14**: 1664
- [5] FU X H, LI C L, ZHANG G L, *et al.* Data processing for the Active Particle-induced X-ray Spectrometer and initial scientific results from Chang'E-3 [J]. *Res. Astron. Astrophys.*, 2014, **14**: 1595
- [6] HE Z P, WANG B Y, LU G, *et al.* Operating principles and detection characteristics of the Visible and Near-Infrared Imaging Spectrometer in the Chang'E-3 [J]. *Res. Astron. Astrophys.*, 2014, **14**: 1567
- [7] LI C L, MU L L, ZOU X D, *et al.* Analysis of the geomorphology surrounding the Chang'E-3 landing site [J]. *Res. Astron. Astrophys.*, 2014, **14**: 1514
- [8] LIN X, OUYANG Z. Scientific progress in China's Lunar Exploration Program [J]. *Chin. J. Space Sci.*, 2014, **34**: 525
- [9] LIU B, LI C L, ZHANG G L, *et al.* [9] Data processing and preliminary results of the Chang'E-3 VIS/NIR Imaging Spectrometer in-situ analysis [J]. *Res. Astron. Astrophys.*, 2014, **14**: 1578
- [10] LIU J J, YAN W, LI C L, *et al.* Reconstructing the landing trajectory of the CE-3 lunar probe by using images from the landing camera [J]. *Res. Astron. Astrophys.*, 2014, **14**: 1530
- [11] REN X, LI C L, LIU J J, *et al.* A method and results of color calibration for the Chang'E-3 terrain camera and panoramic camera [J]. *Res. Astron. Astrophys.*, 2014, **14**: 1557
- [12] SU Y, FANG G Y, FENG J Q, *et al.* Data processing and initial results of Chang'e-3 lunar penetrating radar [J]. *Res. Astron. Astrophys.*, 2014, **14**: 1623
- [13] TAN X, LIU J J, REN X, *et al.* Scientific data products and the data pre-processing subsystem of the Chang'E-3 mission [J]. *Res. Astron. Astrophys.*, 2014, **14**: 1682
- [14] WANG F F, LIU J J, LI C L. A new lunar absolute control point: established by images from the landing camera on Chang'E-3 [J]. *Res. Astron. Astrophys.*, 2014, **14**: 1543

- [15] WEN W B, WANG F, LI C L, *et al.* Data preprocessing and preliminary results of the Moon-based Ultraviolet Telescope on the CE-3 Lander [J]. *Res. Astron. Astrophys.*, 2014, **14**:1674
- [16] ZHANG H B, ZHENG L, SU Y, *et al.* Performance evaluation of lunar penetrating radar onboard the rover of CE-3 probe based on results from ground experiments [J]. *Res. Astron. Astrophys.*, 2014, **14**:1633
- [17] ZHANG J, YANG W, HU S, *et al.* Volcanic history of the Imbrium basin: a close-up view from the lunar rover Yutu [J]. *Proc. Natl. Acad. Sci. USA*, 2015, **112**:5342-5347
- [18] HU S, LIN Y T, LIU B, *et al.* Reflectance calibration and shadow effect of VNIS spectra acquired by the Yutu rover [J]. *Res. Astron. Astrophys.*, 2015, **15**:1587-1596
- [19] XIAO L, ZHU P M, FANG G Y, *et al.* A young multilayered terrane of the northern Mare Imbrium revealed by ChangE-3 mission [J]. *Science*, 2015, **347** (6227):1226-1229
- [20] ZHAO J, HUANG J, QIAO L, *et al.* Geologic characteristics of the Chang'E-3 exploration region [J]. *Sci. China: Phys. Mech. Astron.*, 2014, **57** (3):1-8
- [21] FA W Z, ZHU M, LIU T, *et al.* Regolith stratigraphy at the Chang'E-3 landing site as seen by Lunar Penetrating Radar [J]. *Geophys. Res. Lett.*, 2015. DOI: 10.1002/2015GL066537
- [22] QIAO Le, XIAO Zhiyong, ZHAO Jiannan, XIAO Long. Subsurface structures at the Chang'E-3 landing site: inter-pretations from orbital and in-situ imagery data [J]. *J. Earth Sci.*, 2016. DOI: 10.1007/s12583-015-0655-3
- [23] LING Z C, JOLLIFF B L, WANG A L, *et al.* Correlated compositional and mineralogical investigations at the Chang'E-3 landing site [J]. *Nat. Commun.*, 2015, **6**:8880. DOI:10.1038/ncomms9880
- [24] ZHANG H, YANG Y Z, YUAN Y, *et al.* In-situ optical measurements of Chang'E-3 landing site in Mare Imbrium 1: mineral abundances inferred from spectral reflectance [J]. *Geophys. Res. Lett.*, 2015, **42**:6945-6950
- [25] JIN W D, ZHANG H, YUAN Y, *et al.* In-situ optical measurements of Chang'E-3 landing site in Mare Imbrium 2: photometric properties of the regolith [J]. *Geophys. Res. Lett.*, 2015, **42**: 8312-8319
- [26] HE Fei, ZHANG Xiaoxin, CHEN Bo, *et al.* Moon-based EUV imaging of the Earth's Plasmasphere: model simulations [J]. *J. Geophys. Res.*, 2013, **118**:7085-7103
- [27] Feng J Q, Liu J J, He F, *et al.* Data processing and initial results from the CE-3 Extreme Ultraviolet Camera [J]. *Res. Astron. Astrophys.*, 2014, **14**:1664-1673
- [28] CHEN Bo, SONG Kefei, LI Zhaohui, *et al.* Development and calibration of the Moon-based EUV camera for Chang'E-3 [J]. *Res. Astron. Astrophys.*, 2014, **14**:1654-1663
- [29] ZHENG Chen, PING Jingsong, WANG Mingyuan, *et al.* Geocentric position preliminary detection from the extreme ultraviolet images of Chang'E-3 [J]. *Astrophys. Space Sci.*, 2015, **358**, 2839
- [30] YAN Yan, WANG Huaning, HAN He, *et al.* Analysis of observational data from Extreme Ultra-Violet Camera onboard Chang'E-3 mission [J]. *Astrophys. Space Sci.*, 2016, **361**:76-83
- [31] HE F, ZHANG X X, WANG X Y, CHEN B. EUV emissions from solar wind charge exchange in the Earth's magnetosheath: three-dimensional global hybrid simulation [J]. *J. Geophys. Res.*, 2015, **120**:138156. DOI: 10.1002/2014JA020521
- [32] HE F, ZHANG X X, CHEN B, *et al.* Determination of the Earth's plasmopause location from the CE-3 EUVC images [J]. *J. Geophys. Res.*, 2016, **121**:296-304. DOI:10.1002/2015JA021863
- [33] ZHANG X X, HE F, CHEN B, *et al.* Plasmaspheric evolutions during substorms observed by CE-3 EUVC [J]. *GRL* (under review)
- [34] HE Han, SHEN Chao, WANG Huaning, *et al.* Plasmaspheric evolutions during substorms observed by CE-3 [R]. *Scientific Reports* (under review)
- [35] WANG J, WU C, QIU Y L, *et al.* An unprecedented constraint on water content in the sunlit lunar exosphere seen by Lunar-based Ultraviolet Telescope of Chang'E-3 mission [J]. *Planet. Space Sci.*, 2015, **109**:123
- [36] WANG J, CAO L, MENG X M, *et al.* Photometric calibration of the lunar-based ultraviolet telescope for its first six months of operation on the lunar surface [J]. *Res. Astron. Astrophys.*, 2015, **15**:1068
- [37] WANG J, MENG X M, HAN X H, *et al.* 18-months operation of lunar-based ultraviolet telescope: a highly stable photometric performance [J]. *Astrophys. Space Sci.*, 2015, **360**:10
- [38] QI Z X, YU Y, CAO L, *et al.* Astrometric support for the lunar-based ultraviolet telescope [J]. *Public. Astron. Soc. Pacific*, 2015, **127**:1152
- [39] MENG X M, CAO L, QIU Y L, *et al.* Data processing pipeline for pointing observations of Lunar-based Ultraviolet Telescope [J]. *Astrophys. Space Sci.*, 2015, **358**:47
- [40] QIAN S B, ZHOU X, ZHU L Y, *et al.* LUT reveals a new mass-transferring semi-detached binary [J]. *Astron. J.*, 2015, **150**:193
- [41] ZHU L Y, ZHOU X, HU J Y, *et al.* LUT reveals an algol-type eclipsing binary with three additional stellar companions in a multiple system [J]. *Astron. J.*, 2016, **151**:107
- [42] LIAO W P, QIAN S B, ZEJDA M, *et al.* Lunar-based Ultraviolet telescope study of the well-known Algol-type binary TW Dra [J]. *Res. Astron. Astrophys.*, 2016 (accepted)